

This document is the accepted manuscript version of a published work that appeared in final form in ACS applied materials and interfaces, copyright © American Chemical Society after peer review and technical editing by the publisher.

To access the final edited and published work see:
<https://dx.doi.org/10.1021/acsami.5b00632>.

Published under a “All rights reserved” license.

Surface Modification of TiO₂ Nanocrystals by WO_x Coating or Wrapping: Solvothermal Synthesis and Enhanced Surface Chemistry

Mauro Epifani,^{*,†} Raül Díaz,[‡] Force Carmen,[§] Elisabetta Comini,^{||} Marta Manzanares,[⊥] Teresa Andreu,[⊥] Aziz Genç,[#] Jordi Arbiol,^{#,⊗} Pietro Siciliano,[†] Guido Faglia,^{||} and Joan R. Morante^{⊥,○}

[†]Istituto per la Microelettronica e i Microsistemi, IMM-CNR, Via Monteroni, 73100 Lecce, Italy

[‡]Electrochemical Processes Unit, IMDEA Energy Institute, Avda. Ramón de la Sagra 3, 28935 Móstoles, Spain

[§]NMR Unit, Centro de Apoyo Tecnológico, Universidad Rey Juan Carlos, c/Tulipán, s/n, 28933 Móstoles, Spain

^{||}SENSOR Lab, Department of Information Engineering, Brescia University and CNR-INO, Via Valotti 9, 25133 Brescia, Italy

[⊥]Catalonia Institute for Energy Research, IREC, Universitat de Barcelona, c/Jardins de les Dones de Negre 1, 08930 Sant Adria del Besos, Barcelona, Spain

[#]Institut de Ciència de Materials de Barcelona, ICMAB-CSIC, Campus de la UAB, 08193 Bellaterra, Spain

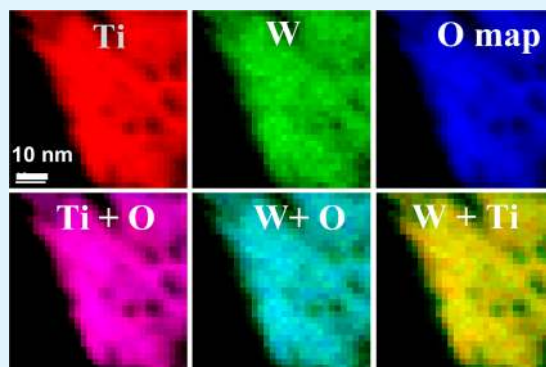
[⊗]Institució Catalana de Recerca i Estudis Avançats (ICREA), Passeig Lluís Companys 23, 08010 Barcelona, CAT Spain

[○]M2E-IN2UB-XaRMAE, Departament d'Electrònica, Universitat de Barcelona, c/Martí i Franquès 1, 08028 Barcelona, Spain

Supporting Information

ABSTRACT: TiO₂ anatase nanocrystals were prepared by solvothermal processing of Ti chloroalkoxide in oleic acid, in the presence of W chloroalkoxide, with W/Ti nominal atomic concentration (R_w) ranging from 0.16 to 0.64. The as-prepared materials were heat-treated up to 500 °C for thermal stabilization and sensing device processing. For $R_{0.16}$, the as-prepared materials were constituted by an anatase core surface-modified by WO_x monolayers. This structure persisted up to 500 °C, without any WO₃ phase segregation. For R_w up to $R_{0.64}$, the anatase core was initially wrapped by an amorphous WO_x gel. Upon heat treatment, the WO_x phase underwent structural reorganization, remaining amorphous up to 400 °C and forming tiny WO₃ nanocrystals dispersed into the TiO₂ host after heating at 500 °C, when part of tungsten also migrated into the TiO₂ structure, resulting in structural and electrical modification of the anatase host. The ethanol sensing properties of the various materials were tested and compared with pure TiO₂ and WO₃ analogously prepared. They showed that even the simple surface modification of the TiO₂ host resulted in a 3 orders of magnitude response improvement with respect to pure TiO₂.

KEYWORDS: TiO₂, solvothermal synthesis, metal oxide nanocrystals, surface modification, gas sensors, nanocomposites



INTRODUCTION

TiO₂–WO₃ composite materials have, for a long time, been known as efficient catalysts for selective catalytic reduction of NO_x,^{1–4} but they have also been used for other reactions such as isomerizations,^{5–7} isopropanol dehydration,⁸ and glycerol conversion,^{9–11} just to mention a few additional examples. Even the photocatalytic properties were well-known,^{12–16} and they have been recently attracting increasing attention.^{17–22} Further applications concern the gas-sensing properties.^{23,24} All these applications rely on a synergistic interaction between the WO_x species and the surface of the TiO₂ support. It is then not surprising that intensive efforts have been devoted in the past to the investigation of the structure of such species as a function of the tungsten concentration, dehydration conditions, heat-treatment temperature, and of all the parameters that may determine their distribution and evolution. In the large majority of these studies, the TiO₂ support was constituted by

commercial P25 samples, or other kind of material typologies,²⁵ where the grain size of the TiO₂ was beyond the nanosized regime,^{25,26} and typical synthesis approaches included coprecipitation and impregnation. Other synthesis procedures were also investigated. Engweiler et al. used grafting of W alkoxides but onto commercial P25 titania.¹ Puddu et al. used hydrothermal synthesis to directly prepare TiO₂–WO₃ nanocomposites.¹⁴ Sol–gel coprocessing of titanium alkoxides and other tungsten precursors was also applied.^{3,15,20,27} The material architecture could anyway be described by titania base material whose surface was covered by WO_x species, possibly not affecting the whole surface for low W concentrations. In these cases, the size of the anatase grains

Received: January 21, 2015

Accepted: March 16, 2015

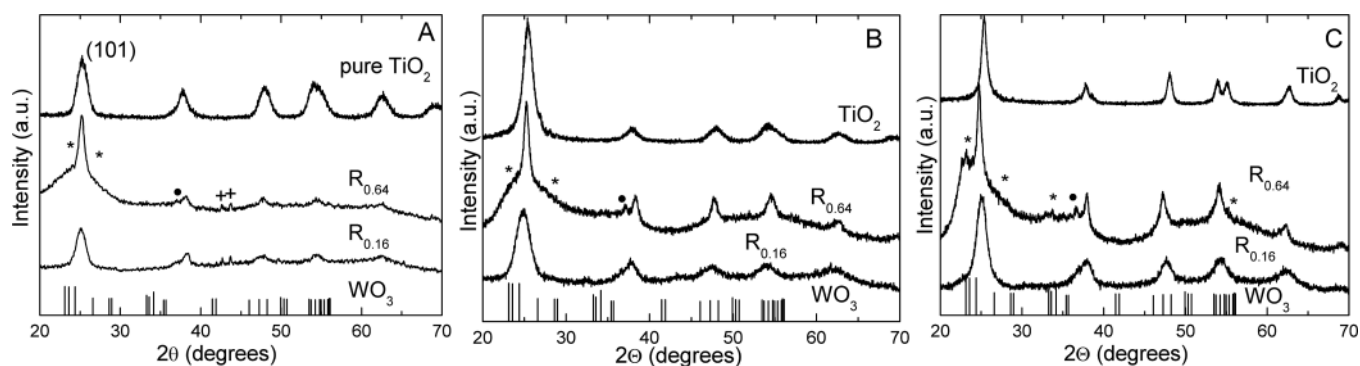


Figure 1. XRD patterns of the as-prepared (A), 400 °C (B), and 500 °C (C) samples. For WO_3 , the positions of the most intense reflections of the monoclinic phase (JCPDS 00–043–1035) are indicated. The symbols indicate the reflections not attributable to anatase (see text).

62 dominates the materials architecture: simply, when the surface
 63 capacity of accommodating tungsten oxide monolayers is
 64 exhausted, the WO_3 particles begin to segregate. It seems
 65 that TiO_2 colloidal nanocrystals, whose size should be
 66 comparable with that of any WO_3 segregated species, have
 67 never been considered as host material. This topic is of
 68 remarkable interest for different reasons. From a fundamental
 69 point of view, we wondered what happens if the TiO_2 support
 70 is constituted by colloidal nanocrystals, whose size becomes
 71 comparable to the segregated WO_3 phase. This question was
 72 suggested by previous work on the TiO_2 – V_2O_5 system,
 73 showing the possibility of coating the surface of anatase
 74 nanocrystals with vanadium oxide species.²⁸ The chemistry of
 75 the vanadium precursor prevented the precipitation of
 76 vanadium oxide grains up to at least 400 °C. The analogous
 77 W precursor has a markedly different chemistry, enhancing the
 78 formation of W oxides.²⁹ Hence, the aim was to explore which
 79 kind of structures could be obtained in this case. We will show
 80 that, with respect to the existing works, the developed synthesis
 81 not only preserves the nanosized TiO_2 base material, but results
 82 in different architectures, ranging from surface modification to
 83 wrapping by WO_x gel. This result has remarkable interest even
 84 from an applicative point of view. We originally developed the
 85 synthesis for gas-sensing field, where it is now well-established
 86 that nanosized oxide grains may remarkably boost the
 87 performance of chemoresistive gas-sensors. Nevertheless, if
 88 the TiO_2 core has remarkably larger size than the WO_x guest
 89 material, the electrical and sensing performance will still be
 90 dominated by those of TiO_2 , since the WO_x phase will only
 91 constitute an extremely thin part of the overall material
 92 structure. The use of colloidal nanocrystalline TiO_2 paves the
 93 way to an enhanced synergistic effect, since now the WO_x
 94 contribution becomes more comparable to the TiO_2 base
 95 material. Indeed, we obtained a fully nanosized version of the
 96 TiO_2 – WO_x catalyst: even after heating at 500 °C, the mean
 97 grain size was 8–10 nm. We will show that electrical and
 98 sensing properties of the resulting materials were remarkably
 99 modified by the presence of the WO_x species, with gas-response
 100 enhancement ranging over orders of magnitude. The success of
 101 the sensing application was meant only to further establish and
 102 develop the approach of inorganic surface modification by
 103 another oxide, which is novel in gas-sensing field and enables
 104 further interesting applications. From a more general point of
 105 view, we will show the effectiveness of coupling an architecture
 106 that is of interest for heterogeneous catalysis itself with a field
 107 like gas sensors where the surface reactions are of primary
 108 importance. Moreover, the set of the obtained results was the

starting point for clarifying the difference between oxide
 heterojunctions and surface monolayers.

EXPERIMENTAL SECTION

The synthesis strategy comprised two steps: first amorphous TiO_2
 nanoparticles were synthesized by sol–gel process,³⁰ and then they
 were crystallized in a solvothermal step where the tungsten precursor
 was also added. The first step was described in detail in previous
 work.²⁸ The following solvothermal crystallization step²⁸ was
 performed for 2 h at 250 °C after dispersing the TiO_2 nanoparticles
 in 10 mL of oleic acid. In this step, a given volume, ranging from 0.5 to
 2 mL, of tungsten chloromethoxide solution was added before the
 solvothermal heating, for preparing TiO_2 – WO_3 materials. The
 tungsten precursor was prepared as described in previous work,²⁹
 starting from WCl_6 and methanol. The W-modified samples will be
 denoted with the R_x code, where x , indicating the nominal W/Ti
 atomic concentration, ranged from 0.16 to 0.64. After the solvothermal
 step, the synthesis product was extracted with methanol and purified
 with acetone.

X-ray diffraction (XRD) patterns, Fourier transform infrared
 (FTIR) and Raman measurements, and thermal analyses were
 obtained with the previously described setup.²⁸

Solid-state NMR spectra of $^{47/49}\text{Ti}$ (22.53 MHz) were obtained
 using a Varian Infinity 400 spectrometer operating at 400 MHz with
 9.395 T, using a probe with a 7 mm coil in static conditions. The
 sequence used to obtain the spectra was two pulses Hahn spin–echo
 with phase cycle. The pulse was 40 μs in duration. The delay between
 scans was 1, and 20,000 scans were collected for each spectrum. The
 titanium NMR spectra were referenced against the standard titanium
 isopropoxide. This compound is shifted (–850 ppm) against the
 conventional shift standard for titanium TiCl_4 (0 ppm).

X-ray photoelectron spectroscopy (XPS) was performed using a
 PHI ESCA-5500 equipment working with the Al $K\alpha$ radiation (1486.6
 eV).²⁸ The powders were fixed on the sample holder with a biadhesive
 tape, giving them a certain amount of surface charging on all of the
 peak positions of the main narrow scan spectra acquired: W 4f, Ti 2p
 and Ti 3p, O 1s, C 1s. They were all properly corrected with respect to
 the adventitious C 1s present on the surface with respect to the
 tabulated and literature value of 284.6 eV.

High-resolution transmission electron microscopy (HRTEM)
 analyses of the powders were obtained with a previously described
 setup,²⁸ consisting in a field emission gun microscope FEI Tecnai F20,
 working at 200 kV and with a point-to-point resolution of 0.19 nm.
 Scanning transmission electron microscopy (STEM) in high angle
 annular dark field (HAADF) mode combined with electron energy
 loss spectroscopy (EELS) spectrum imaging were also obtained in the
 same FEI Tecnai F20.

The gas-sensing tests were performed on the materials heat-treated
 at 500 °C by using the previously described standard configuration for
 resistive sensor measurement and the same fabrication procedure.²⁸
 The sensor devices were placed in a sealed chamber with a constant
 flux of 0.3 L/min of humid synthetic air (40% relative humidity (RH))

160 at 20 °C) into which the desired amount of test gases was mixed. The
 161 sensor response was defined as $(G_{\text{gas}} - G_0)/G_0$, where G_0 was the
 162 sensor baseline electrical conductance in synthetic air, and G_{gas}
 163 indicated the sensor electrical conductance after exposure to the
 164 target gas. Ethanol was tested in concentrations ranging from 50 to
 165 500 ppm. Ethanol is a classical choice as a gas of relevant practical
 166 interest, but above all we wanted a gas to be compared with our
 167 previous $\text{TiO}_2\text{-V}_2\text{O}_5$ work,²⁸ where ethanol had been chosen in
 168 agreement with the organics oxidation activity of $\text{TiO}_2\text{-V}_2\text{O}_5$ classical
 169 catalyst. In this way, the principle of catalytic surface activation by
 170 deposition of another oxide could be tested and possibly reinforced.
 171 The sensing devices selected for the gas tests had base conductance
 172 values dispersed within 10% of the results showed in the manuscript.
 173 In this case, the measured responses were also comprised in such
 174 range. Error bars were hence not included in the plots for the sake of
 175 clarity. Repeated experiments under the same operational conditions
 176 yielded stable and reproducible sensor responses for several months
 177 (estimated uncertainty = $\pm 10\%$). For comparison, the response of
 178 previously investigated devices based on pure TiO_2 ²⁸ and WO_3 ³¹ was
 179 also considered.

180 ■ RESULTS AND DISCUSSION

181 **1. Structure and Structural Evolution of the Materials**
 182 **as a Function of R_w .** The XRD patterns of the as-prepared
 183 samples with various R_w values are reported in Figure 1. Other
 184 R_w values were investigated, but there were no obvious
 185 differences between the related XRD patterns (Figure S1,
 186 Supporting Information), so only $R_{0.16}$ and $R_{0.64}$ were
 187 considered throughout the rest of the work. The pattern of
 188 the $R_{0.16}$ sample was very similar to that of pure TiO_2 , apart for
 189 a few weak additional peaks. The remaining peak positions
 190 were in agreement with those of pure TiO_2 in the anatase
 191 crystallographic phase.

192 The $R_{0.64}$ sample showed, at low angles, additional signals
 193 overlapped with the (101) anatase peak. Other additional
 194 peaks, in the same positions of those observed in the $R_{0.16}$
 195 pattern, are also indicated. The broad, low-angle peaks marked
 196 with a star were in agreement with the JCPDS data for various
 197 WO_x compounds. Nevertheless, only the most intense
 198 reflections of WO_3 and tungsten titanate ($\text{Ti}_{0.54}\text{W}_{0.46}\text{O}_2$,
 199 JCPDS: 98-004-4652) occurred where marked by stars and
 200 a full circle, respectively, in the figure. Other peaks of the
 201 titanates could be overlapped with anatase; anyway, not all of
 202 the expected peaks were observed. After the material was
 203 heated at 400 °C, no different reflections were observed. Only
 204 the peaks indicated with crosses, related to an unidentified
 205 phase in the as-prepared samples, disappeared. After the
 206 material was heated at 500 °C, the main (101) anatase peak was
 207 shifted to lower angles for $R_{0.64}$, while the WO_3 peaks at lower
 208 angles were more resolved, and new ones appeared, indicated in
 209 the figure with further stars. For $R_{0.16}$ only the anatase pattern
 210 was still observed, apart for the additional peak at $2\theta \approx 37^\circ$,
 211 present at all the considered temperatures. For $R_{0.64}$, the
 212 situation was more complex. After the material was heated at
 213 500 °C the (105) and (211) peaks at ca. $53\text{--}55^\circ$ did not split
 214 (Figure 1C), and the (101) peak at $\sim 25^\circ$ was visibly shifted to
 215 lower angles. We note that the tungsten titanate phase,
 216 indicated with a solid circle, was always present, even after
 217 heating at high temperatures, above all for $R_{0.64}$, without
 218 remarkable relative intensity variations.

219 We believe that this phase was a byproduct of the reaction of
 220 the W precursor with the Ti oxide species generated in the
 221 solvothermal step by the dissolution–re-precipitation processes
 222 of the TiO_2 nanoparticles, since (i) formation of such phase
 223 occurred already in the as-prepared materials, where diffusion

of the W^{6+} cations into the anatase structure would be unlikely;
 224 moreover, (ii) should diffusion occur, it would not be
 225 understood why only a small fraction of the titanate phase
 226 was actually present. The Raman spectra of the same samples
 227 were measured, expecting them to be more sensitive to
 228 modifications of the crystal structure. The spectra are shown in
 229 Figure 2. In the as-prepared samples, apart for the anatase
 230

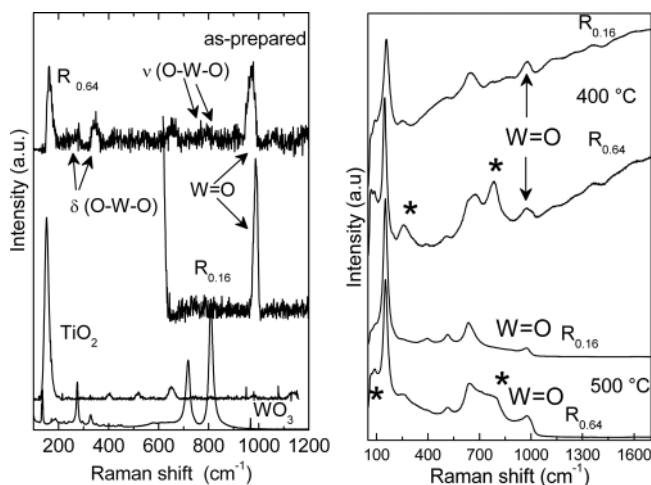


Figure 2. Raman spectra measured on the as-prepared (left), 400 °C, and 500 °C (right) samples. The Raman spectra of pure TiO_2 and WO_3 are reported as a reference in the as-prepared spectra.

231 Raman features, bands at ~ 274 and 330 cm^{-1} were present for
 232 both W concentrations, and more clearly for $R_{0.64}$. They were
 233 attributed³² to the δ (O–W–O) modes, while weak bands
 234 overlapped to the background in the 800 cm^{-1} region suggest
 235 the ν (O–W–O) modes. Finally, a strong band was observed
 236 at 1007 and 974 cm^{-1} for $R_{0.16}$ and $R_{0.64}$, respectively. For $R_{0.16}$,
 237 the 1007 cm^{-1} band could be observed only when the rest of
 238 the anatase signal saturated; hence, the complete spectrum is
 239 shown in the Supporting Information (Figure S2).

240 The band is due to the W=O stretching mode of surface-
 241 dispersed tungsten oxide species.^{1,33–40} The position and
 242 evolution of this band can give useful hint about the surface
 243 WO_x surface coverage, as we will see in the following. Hence,
 244 we will focus our attention to its position, which is summarized
 245 in Table 1 for all the samples. For completeness, we will only
 246 further remark on the non-anatase bands in heat-treated
 247 samples, which were marked by a star in Figure 2 (right). First
 248 of all, bands appeared at low frequency in similar positions to

Table 1. W=O Raman Position for the Indicated Samples

sample	W=O position (cm^{-1})	attribution
as-prepared $R_{0.16}$	1007	tetrahedral W species
as-prepared $R_{0.64}$	974	tetrahedral and octahedral W species
400 °C $R_{0.16}$	950	tetrahedral and octahedral W species, increased fraction of octahedral sites
400 °C $R_{0.64}$	950	tetrahedral and octahedral W species, increased fraction of octahedral sites
500 °C $R_{0.16}$	974	tetrahedral and octahedral W species
500 °C $R_{0.64}$	974	tetrahedral and octahedral W species

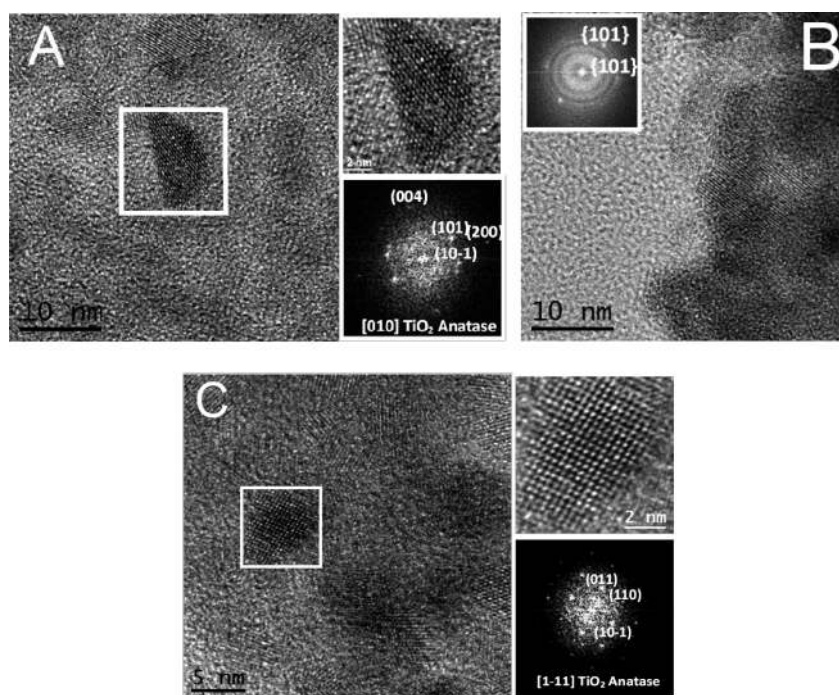


Figure 3. HRTEM images of as-prepared (A) $R_{0.16}$, (B) $R_{0.64}$, and 500 °C (C) $R_{0.16}$ samples. The insets show magnifications of the white-squared regions, with the related power spectra.

lattice modes of WO_3 (below $\sim 100 \text{ cm}^{-1}$). A broad and strong band was found in the δ (O–W–O) region at $\sim 250 \text{ cm}^{-1}$ and, for $R_{0.64}$, at 785 cm^{-1} , in the ν (O–W–O) region. Moreover, after heating at 500 °C, there was no more organic residuals signal. Figure 3 shows representative TEM observations of as-prepared and 500 °C samples. The structure found in the as-prepared $R_{0.16}$ sample was TiO_2 tetragonal anatase. In the analogous $R_{0.64}$ sample, surprisingly, HRTEM showed that the material was composed of small amorphous clusters. HRTEM did not show crystal planes in any of the small nanostructures (nanoparticle-like). Only in rare cases we could find some crystallized regions showing anatase-like plane distances.

The 500 °C $R_{0.16}$ sample comprised micron/submicron sized agglomerates (due to the thermal elimination of the organic capping) of ca. 7–10 nm spheroidal nanoparticles. Figure 3C shows a general HRTEM micrograph where different single crystalline nanoparticles in the agglomerate are present. Upper right is a close-up of a 10 nm single crystalline nanoparticle, and lower right is its corresponding power spectrum (FFT), which reveals that this nanoparticle has a TiO_2 anatase phase (space group = $I4_1/amd$) with lattice parameters of $a = b = 0.3785 \text{ nm}$ and $c = 0.9514 \text{ nm}$ and viewed along $[1-11]$ direction. Obviously, even the 500 °C $R_{0.64}$ sample comprised micron/submicron sized agglomerates, with $\sim 10 \text{ nm}$ spheroidal nanoparticles, as shown in the Supporting Information. The most surprising result was that the segregated WO_3 nanocrystals could not be distinguished into the TiO_2 host. On the other hand, the obtained d -spacing values could also fit for a monoclinic WO_3 phase, but the error margin as much larger for the case of WO_3 phase (fitting error is 8%). So, TiO_2 phase with a fitting error of $\sim 3\%$ was more likely. This 3% error was due to measured d -spacing values that were larger than those of TiO_2 anatase phase, which might suggest the formation of doped TiO_2 , solid solutions, or even new phases.

The formation of different oxides had already been suggested by the XRD patterns, so XPS was employed for analyzing more

in detail the oxidation states of W in the as-prepared samples. Tungsten has different possible oxidation states, W^{6+} being the most common, but easily presenting substoichiometric oxides such as $\text{W}_{18}\text{O}_{49}$ or $\text{W}_{25}\text{O}_{73}$. W 4f has a spin–orbit doublet ($4f_{7/2}$ and $4f_{5/2}$) with intensity ratio 4:3 (fixed parameter), change in binding energy (ΔBE) of 2.1 eV (fixed parameter), and full width at half-maximum (fwhm) value of 1.6 eV (fixed parameter) except for the substoichiometric $4f_{7/2}$ contribution, which has an expected value of $\sim 1.8 \text{ eV}$. Then, four contributions from the W 4f were used, with expected BE values at 35.5 and 37.6 eV (for WO_3) and 34.3 and 36.5 eV (for WO_x species).^{41,42} Titanium presents also a photopeak in the same energy range (Ti 3p has a BE $\approx 37.0 \text{ eV}$) and was also included as a contribution in the fitting process.^{43,44} Additionally to W 4f contribution, a component corresponding to the W 5p3/2 peak must be factored. The W 5p3/2 peak was set at 5.5 eV above the W 4f7/2 peak. Finally, the shape of the spectra suggested the presence of a tungsten–titanium mixed phase ($\text{W}_x\text{Ti}_y\text{O}_z$) with two photopeaks at ~ 39.0 and 42.0 eV . Summarizing, W 4f spectra were fitted through eight contributions, and the results are reported in Table 2. The figures and the related fits are reported in the Supporting

Table 2. Results of the XPS Fitting on the Indicated Samples

band	as-prepared $R_{0.16}$			as-prepared $R_{0.64}$		
	BE (eV)	fwhm	%area	BE (eV)	fwhm	%area
W^{6+} ($4f_{7/2}$)	34.25	1.85	5.28	34.25	1.9	9.33
W^{6+} ($4f_{5/2}$)	35.55	1.65	38.68	35.46	1.67	39.06
W^{6+} ($4f_{5/2}$)	36.35	1.65	3.96	36.35	1.67	7
Ti 3p	36.95	1.6	8.61	36.95	1.65	5.35
W^{6+} ($4f_{5/2}$)	37.65	1.65	29.01	37.56	1.67	29.29
Ti–O–W	38.95	2.1	10.43	38.95	2.05	6.78
W 5p3/2	41.05	2.08	2.47	41.05	1.95	2.34
Ti–O–W	42.05	2.3	1.56	42.05	2.25	0.86

Information, together with the full results for Ti 2p. The ratio W^{6+}/W^{n+} for each individual peak 4f7/2 and 4f5/2 is 7.3 for $R_{0.16}$ and 4.2 for $R_{0.64}$, indicating that the amount of W^{n+} is higher in the $R_{0.64}$ sample. The relative intensity of Ti 3p peak is lower for $R_{0.64}$, which is consistent with the higher content of W in the sample. The relative amount of tungsten–titanium mixed phase is higher for the $R_{0.16}$ sample. After the XPS results, we will describe the tungsten oxide phases found in the present work with the generic formula WO_x .

On the basis of the experimental data described, we could describe the materials evolution as follows. The as-prepared samples were constituted (XRD) by anatase nanocrystals mixed, for $R_{0.64}$, with amorphous and/or very small tungsten oxide species, whose structure resembled that of monoclinic WO_3 . Figure 3B clarifies that, for $R_{0.64}$, the anatase nanocrystals, whose presence could only be ensured by the results of Figures 1 and 2, were “wrapped” by amorphous WO_x species, which occurred due to the high W concentration. In fact, the XPS data in Table 2 for $R_{0.64}$, for which the Ti/W signal ratio was less than one, clearly indicate that the TiO_2 nanocrystals are buried into the WO_x gel. We use the WO_x description in agreement with the indications of the XPS data, where it appeared that the $R_{0.64}$ sample contained a higher concentration of substoichiometric W species (with respect to WO_3). For $R_w = 0.64$, the outer regions of the WO_x aggregates are less influenced by the presence of the TiO_2 core, and their composition resembles that of chloroalkoxide-derived tungsten oxides, where the presence of substoichiometric species is typical.²⁹ The TiO_2 wrapping is an interesting phenomenon and was made possible by the remarkable hydrolytic instability of the W chloroalkoxide, whose molecules may self-cross-link instead of bonding to the anatase surface. On the other hand, in the same experimental solvothermal conditions, we could synthesize pure WO_3 quantum dots in the monoclinic phase, with a mean size of 4 nm.³¹ From these observations, we concluded that phase separation of W oxide species occurred in the solvothermal step due to self-polymerization of the W precursor, but the TiO_2 nanoparticles interfered with the formation of the WO_3 structure, resulting in smaller species (very broad XRD reflections) whose composition was not the conventional WO_3 oxide. The Raman data allowed clarifying more in detail the structure of the as-prepared samples. The most prominent features of Figure 2A were the surface $W=O$ stretching bands at 1007 cm^{-1} for $R_{0.16}$ and at 974 cm^{-1} for $R_{0.64}$. The position depends on the W local coordination.³⁴ As summarized in Table 1, peaks above 980 cm^{-1} in the hydrated environment of the present work were attributed to tetrahedral WO_4 species.³⁴ Hence, for $R_{0.16}$ the surface was covered with $W=O$ species with distorted tetrahedral geometry. The band position for $R_{0.64}$, instead, suggested a more complex environment, including distorted octahedral sites, as previously discussed for high-coverage case,³⁴ to which the $R_{0.64}$ case could be assimilated. Octahedral sites are in agreement with the gel-like WO_x layer, with higher extent of cross-linking. In fact, the (O–W–O) modes in the Raman spectra corroborated the view of a dense layer of WO_x . In particular, it seemed reasonable to attribute the stronger signal of the bending modes with respect to the stretching ones to the two-dimensional structure of the WO_x layer. In the XPS data, the more intense Ti–O–W signal in $R_{0.16}$ with respect to $R_{0.64}$ was attributed to the signal attenuation due to the anatase wrapping by WO_x . In this frame, further magic-angle spinning NMR data (Supporting Information) supported a view where the anatase nanocrystals had an

increasingly affected surface with increasing W concentration, in such a way that for $R_{0.16}$ the Ti signal was slightly more defined, while for $R_{0.64}$ their local coordination was modified due to the presence of more layers of WO_x .

Summarizing: the reaction with the W chloroalkoxides provided the anatase nanocrystals with a layer of WO_x species. Such species had a tetrahedral environment and were bonded to the surface through Ti–O–W bonds. For $R > 0.16$, the surface was saturated, and the WO_x structures formed an amorphous layer around anatase. The cross-linking of the layer allowed the W cations to assume even octahedral environment through the formation of small and poorly polymerized species.

After they were heated at $400\text{ }^\circ\text{C}$, the samples basically kept their structure (XRD). Above all, for $R_{0.64}$ the amorphous WO_x component persisted. Raman spectra show that the WO_x layer onto the anatase nanocrystals changed its structure, giving rise to a $W=O$ Raman band at 961 cm^{-1} for $R_{0.16}$ and at 951 cm^{-1} for $R_{0.64}$. For high surface coverage, like that in the present work, these bands indicate a mixed environment of tetrahedral and octahedral sites.³⁴ In particular, the downshift of the $W=O$ stretching with respect to the as-prepared samples for both R_w values indicated increased concentration of octahedral sites and, hence, more dense and cross-linked W oxide structures. This is in agreement with the appearance of the new “lattice” bands at very low frequencies and the intense bending band at $\sim 250\text{ cm}^{-1}$. We finally note the rising background toward high frequencies, due to the organic residuals still present in the samples. In fact, they appeared bright brownish after the heat treatment, and FTIR spectra (discussed below) suggested the application of higher-temperature treatments. Moreover, the Raman spectra presented broad bands at ~ 1400 and 1600 cm^{-1} , which are typical of graphite species, compatible with ongoing organics decomposition during the heat treatment.^{45–47} Summarizing: the heat treatment at $400\text{ }^\circ\text{C}$, also due to the attenuation of the oleic acid capping, favored the cross-linking and densification of the WO_x phases for $R_{0.16}$ and $R_{0.64}$. The peculiar structure of the latter was confirmed by the complete absence of crystallization phenomena, very different from pure WO_3 nanocrystals prepared by the same precursor.³¹

After the sample was heated at $500\text{ }^\circ\text{C}$, the WO_x wrapping for $R_{0.64}$ was finally crystallized, as seen by XRD (Figure 1C), while for $R_{0.16}$ the surface layer of W oxide did not undergo obvious changes, demonstrating remarkable stability up to high temperatures. The presence of the surface layer had further consequence in the limitation of the grain growth, since the samples showed less enhanced peak narrowing with respect to pure TiO_2 . The high-temperature treatment affected even the TiO_2 structure, as seen by the shift to lower angles of the XRD anatase peaks (Figure 1C). The Raman spectra confirmed the XRD interpretation. The structural modification induced by W was reflected in the shape of the anatase Raman bands, through their broadening and distortion, mainly for $R_{0.64}$, but it must be remarked that in all cases the Raman spectrum showed changes with respect to pure TiO_2 . The position of the $W=O$ Raman band was 974 cm^{-1} for both samples, indicating further redistribution of the W sites, in agreement with the XRD results. The main doubt concerned the fate of the amorphous WO_x layer for $R_{0.64}$ and its interaction with the anatase host material.

For further investigating this point, which was needed since the organics elimination and subsequent device processing required such $500\text{ }^\circ\text{C}$ treatment, EELS investigation was performed on the corresponding sample. In Figure 4, a general

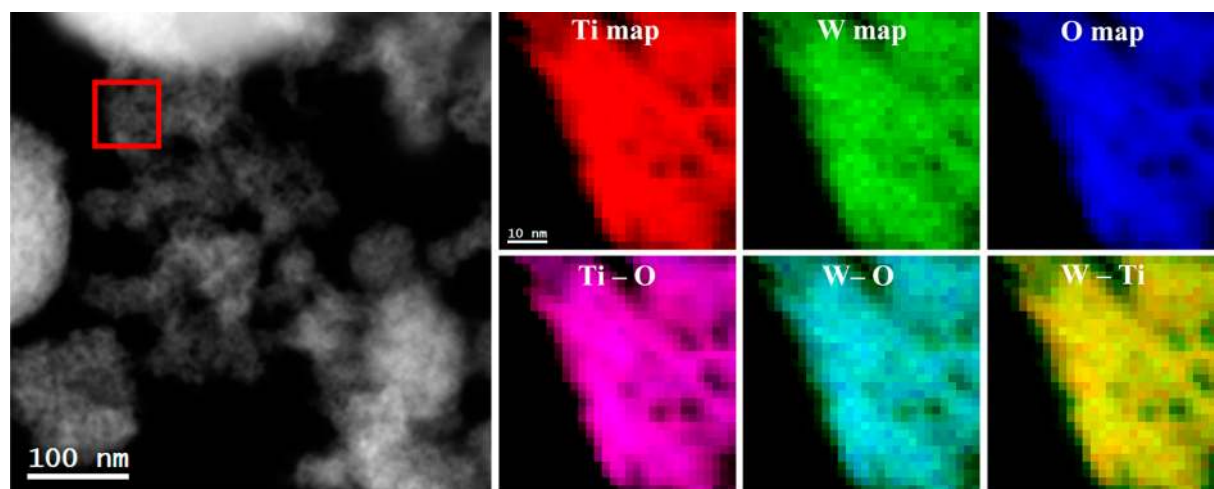


Figure 4. A general STEM-HAADF micrograph and EELS maps of the red squared region: elemental Ti (red), W (green), and O (blue) maps and, in the bottom part, from left to right, composites of Ti–O, W–O, and W–Ti.

433 STEM-HAADF micrograph and elemental EELS maps of the
 434 red squared region are presented. As seen in the color maps,
 435 the Ti, W, and O are distributed almost homogeneously
 436 throughout the nanoparticles. This result showed that after the
 437 heat-treatment at 500 °C the crystallized WO₃ material
 438 remained distributed over the TiO₂ phase, possibly resembling
 439 the previous wrapping structure. Nevertheless, it was difficult to
 440 directly visualize the WO₃ structures, as discussed for Figure 3.
 441 Because of the found differences in the TiO₂ lattice parameters,
 442 in agreement with the shift of the XRD peaks, it was concluded
 443 that part of tungsten diffused into the TiO₂ phase, as reinforced
 444 by the electrical data shown below. The WO₃ nanocrystals, as
 445 indicated by the related peaks in the XRD pattern in Figure 1C,
 446 may just be too small to be detected in the mass of the anatase
 447 host, which agglomerated after the removal of the oleic acid
 448 capping. The results shown introduce a remarkable difference
 449 with respect to previous works. In fact, the use of anatase
 450 nanocrystals, with a size that initially ranges ~3 nm in the as-
 451 prepared samples, allowed complete wrapping by the gel-like
 452 WO_x component for R_{0.64}. This effect could obviously not be
 453 obtained with larger-sized TiO₂ materials. Summarizing: the
 454 heat treatment at 500 °C did not change the structure of the
 455 R_{0.16} samples, still constituted by anatase nanocrystals that were
 456 surface-modified with WO_x, which did not undergo any phase
 457 segregation. The R_{0.64} material was composed by a dispersion of
 458 tiny WO₃ nanocrystals around the surface-modified TiO₂ host.
 459 The TiO₂ itself was structurally modified by W doping. As a
 460 whole, changing the W concentration and using proper heat-
 461 treatment procedure, allowed exploration of a range of material
 462 architectures from naked anatase to surface coverage to
 463 heterojunctions.

464 **2. Thermal Behavior of the Materials.** Device processing
 465 requires heat treatment for thermal stabilization, since chemo-
 466 resistive gas sensors may require high-temperature operation,
 467 and hence prestabilization at a temperature higher than the
 468 maximum predicted operation conditions. Moreover, elimi-
 469 nation of any organic residual is required for having a stable
 470 electric signal and improving the conductance. Optimization of
 471 the heat-treatment procedure may be performed by thermal
 472 analysis and checked by FTIR and Raman spectroscopy. While
 473 this topic is closely related to the device processing step and
 474 may be considered as a technological step, it also provided
 475 useful hints about the sample structure, so it will now be

discussed in more detail. Figure 5 shows the results of the 476
 thermal analyses performed on the samples with different R_w 477

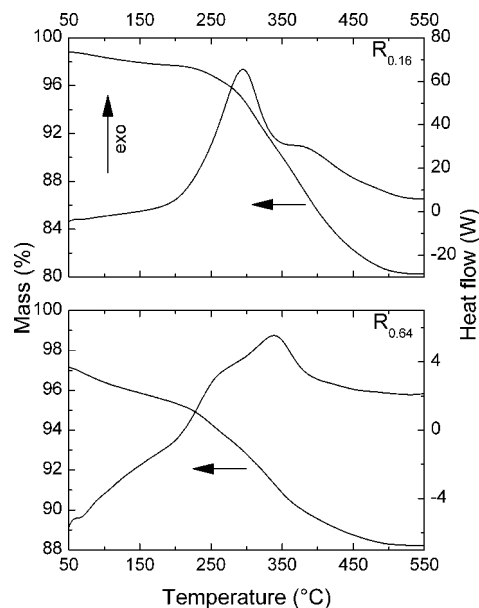


Figure 5. DSC-TG curves measured on the indicated samples. The mass variation is expressed as percentage of the initial value.

values. For both samples, the mass loss reached a plateau at 478
 ~500 °C, which suggested the correct temperature for heat 479
 treatment. As seen in the Raman section, this temperature 480
 ensured the absence of even graphitic carbon from organic 481
 pyrolysis. The thermogravimetric (TG) curve for R_{0.64} had a 482
 more complex structure than that of R_{0.16}, reflecting the shape 483
 of the differential scanning calorimetry (DSC) analysis, 484
 composed of broad, overlapped peaks. 485

Instead, the DSC value of the R_{0.16} sample more closely 486
 resembled that of pure TiO₂.²⁸ These results were in agreement 487
 with a sample structure that, for R_{0.16}, was still basically 488
 constituted by anatase nanocrystals, while that for R_{0.64} was 489
 remarkably affected by the structural evolution of the WO_x 490
 wrapping. In previous work on pure WO₃,³¹ it was evidenced 491
 that the oleic acid capping was labile and easily eliminated even 492
 during the postsynthesis purification step. In the R_{0.64} sample, 493

494 hence, lower concentration of oleic acid would be initially
 495 present, since oleic acid will weakly coordinate to the WO_x
 496 wrapping layer. This explained that the overall mass loss for
 497 $R_{0.16}$ was larger than for $R_{0.64}$, due to the elimination of a larger
 498 concentration of the bulky oleic acid molecules. The IR spectra,
 499 shown in Figure 6, nicely confirmed the interpretation of the

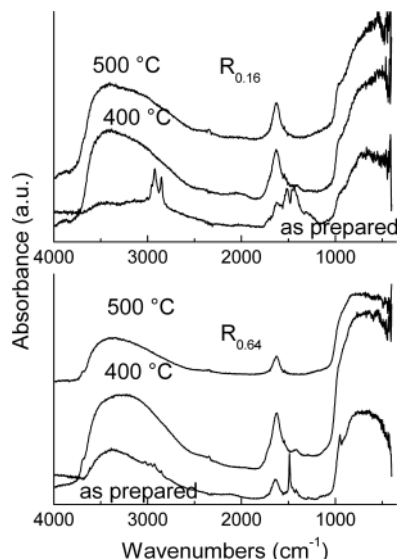


Figure 6. FTIR spectra measured on the $R_{0.16}$ and $R_{0.64}$ samples heat-treated at the indicated temperatures.

500 thermal data. From the device point of view, the organics
 501 elimination occurs after heating at 500 °C. But, above all, the
 502 alkyl bands in the as-prepared $R_{0.64}$ sample at $\sim 3200\text{ cm}^{-1}$ (due
 503 to oleic acid) were almost absent, contrarily to the bands
 504 observed with $R_{0.16}$. Moreover, the OH signal in the as-prepared
 505 $R_{0.16}$ sample was much weaker than in the analogous $R_{0.64}$
 506 spectrum: the more complex condensation and dehydration
 507 phenomena in $R_{0.64}$ were in agreement with the presence of
 508 various peaks and shoulders in the thermal data. The region
 509 around 1500 cm^{-1} contains characteristic features of the oleic
 510 acid molecule. In particular, the absence of the intense carbonyl
 511 band at 1709 cm^{-1} indicates the absence of dimeric oleic acid
 512 molecules (weak shoulders were observed in the 400 °C
 513 spectra, probably indicating residuals of free oleic acid not
 514 bonded to the surface) and complex formation through
 515 bridging/chelating modes.^{48–50}

516 The separation, Δ , between the antisymmetric and
 517 symmetric stretching modes of the carboxylate ion in the
 518 1500 cm^{-1} is useful for determining the type of coordination
 519 bonding.⁵¹ In our case for both samples the Δ value was about
 520 70 cm^{-1} , indicating a mixture of both configurations, in
 521 agreement with the presence of W species with different local
 522 symmetry onto the surface.

523 **2. Gas-Sensing Properties of the Materials.** The
 524 material architectures enabled by the synthesis process spanned
 525 a broad range of configurations, given the same TiO_2 guest
 526 phase, and the related sensing properties were investigated.
 527 Ethanol was chosen as a sample of reducing gas, capable of
 528 increasing the electrical conductance of the materials upon the
 529 sensing process. In Figure 7 the dynamic response curves of the
 530 $R_{0.16}$ and $R_{0.64}$ materials heat-treated at 500 °C are reported,
 531 together with the analogous curves for pure TiO_2 and WO_3 .
 532 First of all, we observe that pure TiO_2 and the $R_{0.16}$ sample had

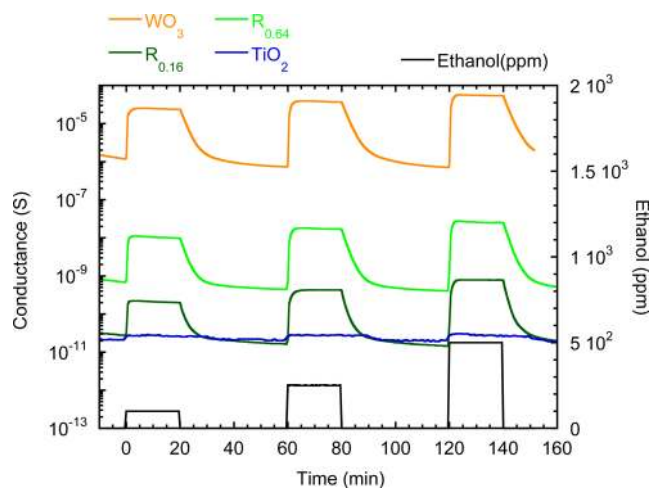
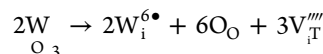
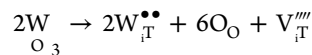


Figure 7. Dynamic response of the indicated sensors toward square concentration pulses of ethanol at a working temperature of 200 °C and 40% RH at 20 °C.

533 very similar base electrical conductance, at about $1 \times 10^{-11}\text{ S}$.
 534 Instead, the $R_{0.64}$ sample had much higher conductance, by ~ 2
 535 orders of magnitude.

536 This result is in agreement with the previously developed
 537 structural interpretation of the samples. In particular, the
 538 incorporation equations in Kröger–Vink notation are the
 539 following, for substitutional and interstitial WO_3 incorporation,
 540 respectively.



541 where W_{Ti} and W_i indicate substitutional and interstitial W(VI)
 542 ions, V_{Ti} is a Ti vacancy, and O_O is an oxygen ion in regular
 543 lattice site. It can be seen that the formation of interstitial
 544 species requires the formation of a larger concentration of
 545 highly charged and energetically unfavorable Ti vacancies.
 546 Substitutional W(VI), whose presence in the $R_{0.64}$ sample was
 547 suggested by the modification of the structural parameters of
 548 TiO_2 and by the peak shift in the XRD patterns, would instead
 549 result in conductance increase by ionization of the loosely
 550 bound extra electrons in the anatase lattice. It is also striking
 551 that, by addition of only the WO_x surface layer for $R_{0.16}$, the
 552 electrical signal underwent a dramatic change upon ethanol
 553 introduction in the cell, differently from pure TiO_2 that
 554 displayed very weak variations. A similar effect occurred for
 555 $R_{0.64}$, having a different composition and structure from $R_{0.16}$.

556 The different responses were calculated and are displayed in
 557 Figure 8 for various operating temperatures. Note that, first of
 558 all, pure TiO_2 response slowly increased with increasing
 559 operating temperature. This trend was opposite to that of the
 560 TiO_2 – WO_3 materials and evidenced catalytic effect of the WO_x
 561 surface modification, featuring low-temperature activation of
 562 the sensing reactions. Hence, 200 °C resulted as the best
 563 operating temperature, where the W-modified materials
 564 provided the highest responses and simultaneous lowering of
 565 power consumption, in contrast to pure TiO_2 , which was
 566 almost inactive at this temperature.

567 The response improvement of 2 orders of magnitude with
 568 respect to pure TiO_2 was the required proof of concept about
 569 the effectiveness of the W-surface modification. This situation

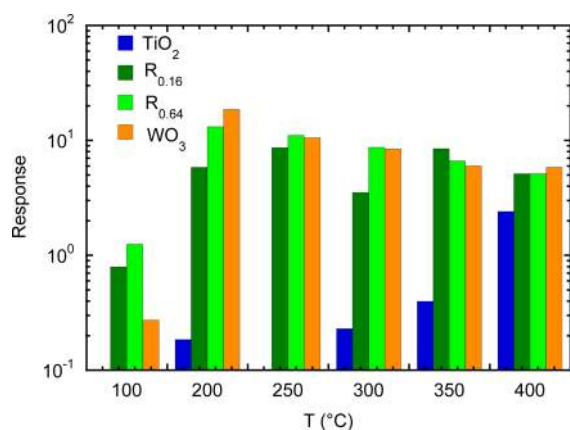


Figure 8. Response to 100 ppm of ethanol as a function of the operating temperature for the indicated sensors.

was also confirmed for different ethanol concentrations at the best operating temperature of 200 °C, as shown in the calibration curves in Figure 9. The curves follow the typical

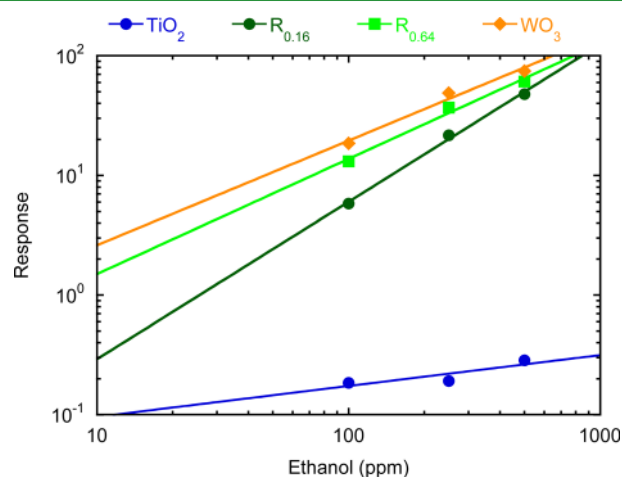


Figure 9. Calibration curve for ethanol of the indicated sensors at a working temperature of 200 °C.

power law⁵² for chemoresistive gas sensors, giving a straight line on double logarithmic scale. What changes, apart for the already observed lower responses for pure TiO₂, is the slope of the curves. Both responses and slopes are grouped for pure WO₃ and the TiO₂–WO_x sensors; only, for R_{0.16} the responses are slightly lower. Since the slope is related to the involved sensing mechanisms, the three materials have markedly different behavior from pure TiO₂: the proposed mechanism for ethanol sensing by SnO₂, based on a previous work by Kohl in 1991,^{53,54} seems applicable, at least as an initial working hypothesis, and it is based on the formation of surface ethoxy groups and their transformation into acetaldehyde, which is then desorbed with hydrogen, or into rooted acetate groups. In our case, then, the surface W=O species would be favorable adsorption sites for ethanol, but we cannot exclude that the presence of W may induce different reaction pathways. In fact, the introduction of tungsten enhanced the sensing behavior of pure TiO₂ by providing its surface with species that, from the sensing point of view, were similar to pure WO₃. As we shall see below, the WO₃ nanocrystals in the R_{0.64} may contribute to the increase of the base conductance and to the ethanol sensing,

but the overall sensing properties for both W-modified sensors were dominated by the TiO₂ surface modification. Further hints about the role of the various components of the obtained materials could be obtained from the analysis of simple electrical properties. The related data are shown in Figures 10

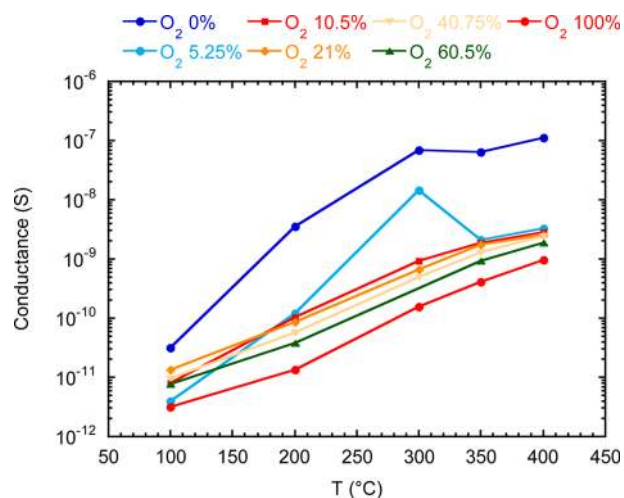


Figure 10. Electrical conductance data of the R_{0.16} sample heat-treated at 500 °C as a function of the operating temperature and oxygen concentration.

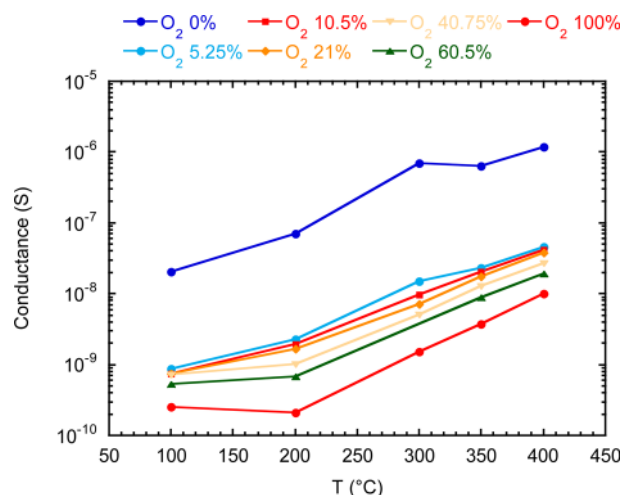


Figure 11. Electrical conductance data of the R_{0.64} sample heat-treated at 500 °C as a function of the operating temperature and oxygen concentration.

and 11 for R_{0.16} and R_{0.64}, respectively. The data have some common features, such as the increasing conductance with increasing temperature, in agreement with the n-type character of the prepared TiO₂-based materials, and a conductance decrease with increasing the oxygen concentration, for a given temperature, due to the oxygen adsorption/ionosorption and the consequent charge extraction from the materials conduction band. More interestingly, the oxygen introduction in the cell resulted in maximum conductance drops ranging ~3 orders of magnitude for both materials, at temperature starting from 200 °C, where additional adsorption phenomena (preadsorbed water, for instance) are less likely. This behavior is much different from that of pure TiO₂,⁵⁵ which is much less sensitive

612 to oxygen concentrations and resembles much more that of
613 pure WO_3 .³¹ On the other hand, the W incorporation
614 equations show that the concentration of oxygen vacancies
615 should be unaffected. So we conclude that the surface oxygen
616 adsorption properties, which are fundamental in the gas-sensing
617 behavior, are dominated by the presence of the W cations in the
618 surface WO_x monolayers.

619 If we observe the conductance variations for both kinds of
620 samples, for a given temperature and oxygen concentration, and
621 keep into account the W doping for $R_{0.64}$, it seems that the
622 WO_3 nanocrystals have a weak electrical effect in the $R_{0.64}$
623 sample, probably mainly acting as a baseline raising the
624 conductance values with respect to $R_{0.16}$. The slightly higher
625 response of the $R_{0.64}$ device may then be influenced by a similar
626 additive term coming from the WO_3 nanocrystals.

627 ■ CONCLUSIONS

628 The crystallization solvothermal processing of amorphous TiO_2
629 nanoparticles can be performed in the presence of a W
630 chloromethoxide, whose concentration allows modifying the
631 structure of the final product from surface modified to WO_x
632 wrapped anatase TiO_2 . The subsequent heat treatment results
633 again in the surface-modified TiO_2 or in a dispersion of WO_3
634 nanocrystals into the TiO_2 guest phase, whose structure is
635 further doped by W cations. From the analysis of the ethanol
636 sensing and basic electrical data, it can be concluded that the
637 surface modification of TiO_2 by monolayers of WO_x species
638 activates the naked anatase species toward the oxidation of
639 ethanol, while the WO_3 dispersed nanocrystals have an additive
640 effect, improving the overall electrical conduction and providing
641 additional gas response. We would finally like to comment
642 about the choice between surface modification and hetero-
643 junctions. Surface modification in $R_{0.16}$ materials provided
644 slightly lower sensing responses than those in $R_{0.64}$. On the
645 other hand, the structure of $R_{0.16}$ was simpler than that of $R_{0.64}$,
646 never featuring WO_3 phase segregation, even after heat
647 treatment at 500 °C. This means that $R_{0.16}$ materials are
648 intrinsically more stable than $R_{0.64}$, where the occurred phase
649 segregation could induce further long-term modifications, such
650 as growth of the WO_3 nanocrystals by coalescence, or by
651 adsorption of W atoms from the TiO_2 nanocrystals. Moreover,
652 the analysis of the data showed that for $R_{0.64}$ the response was
653 slightly affected by the effect of a mechanical mixing of two
654 phases, despite being on a very intimate size scale. Synergistic
655 effects could only be attributed to anatase surface modification,
656 present for both W concentrations, where the surface WO_x
657 species create a more favorable oxidation/conductive channel
658 with respect to pure TiO_2 . Hence, the concept of
659 heterojunction seems to be more applicable, in terms of
660 defining a novel material architecture when real synergistic
661 effects are present, than the simple physical proximity of two
662 distinct phases.

663 ■ ASSOCIATED CONTENT

664 ■ Supporting Information

665 Further XRD patterns of as-prepared materials, complete
666 Raman spectrum of the as-prepared $R_{0.16}$ sample, XPS spectra
667 and data of the as-prepared materials, HRTEM of the 500 °C,
668 $R_{0.64}$ sample, and NMR of as-prepared samples. This material is
669 available free of charge via the Internet at <http://pubs.acs.org>.

■ AUTHOR INFORMATION

Corresponding Author

*E-mail: mauro.epifani@le.imm.cnr.it.

Notes

The authors declare no competing financial interest.

■ ACKNOWLEDGMENTS

Authors acknowledge CSIC/CNR Project No. 2010IT0001
(SYNCAMON) and the SOLAR Project No. DM19447. We
thank G. B. Pace for the help with the sample preparation, and
N. Poli for the help with the sensing measurements.

■ REFERENCES

- (1) Engweiler, J.; Harf, J.; Baiker, A. WO_x/TiO_2 Catalysts Prepared
by Grafting of Tungsten Alkoxides: Morphological Properties and
Catalytic Behavior in the Selective Reduction of NO by NH_3 . *J. Catal.*
1996, *159*, 259–269.
- (2) Forzatti, P.; Lietti, L. Recent Advances in De-NO(x)ing Catalysis
for Stationary Applications. *Heterog. Chem. Rev.* **1996**, *3*, 33–51.
- (3) Zhang, H.; Han, J.; Niu, X. W.; Han, X.; Wei, G. D.; Han, W.
Study of Synthesis and Catalytic Property of WO_3/TiO_2 Catalysts for
NO Reduction at High Temperatures. *Chem.—Eur. J.* **2011**, *350*, 35–
39.
- (4) Wachs, I. E.; Kim, T.; Ross, E. I. Catalysis Science of the Solid
Acidity of Model Supported Tungsten Oxide Catalysts. *Catal. Today*
2006, *116*, 162–168.
- (5) Hino, M.; Arata, K. Superacids by Metal Oxides. 5. Synthesis of
Highly Acidic Catalysts of Tungsten-Oxide Supported on Tin Oxide,
Titanium-Oxide, and Iron-Oxide. *Bull. Chem. Soc. Jpn.* **1994**, *67*,
1472–1473.
- (6) Lebarbier, V.; Clet, G.; Houalla, M. Relations between Structure,
Acidity, and Activity of WO_x/TiO_2 : Influence of the Initial State of the
Support, Titanium Oxyhydroxide, or Titanium Oxide. *J. Phys. Chem. B*
2006, *110*, 22608–22617.
- (7) Patrono, P.; Laginestra, A.; Ramis, G.; Busca, G. Conversion of 1-
Butene over $\text{WO}_3\text{-TiO}_2$ Catalysts. *Appl. Catal., A* **1994**, *107*, 249–266.
- (8) Onfroy, T.; Lebarbier, V.; Clet, G.; Houalla, M. Quantitative
Relationship between the Nature of Surface Species and the Catalytic
Activity of Tungsten Oxides Supported on Crystallized Titania. *J. Mol.*
Catal. A: Chem. **2010**, *318*, 1–7.
- (9) Ulgen, A.; Hoelderich, W. F. Conversion of Glycerol to Acrolein
in the Presence of WO_3/TiO_2 Catalysts. *J. Mol. Catal. A: Chem.* **2011**,
400, 34–38.
- (10) Akizuki, M.; Oshima, Y. Kinetics of Glycerol Dehydration with
 WO_3/TiO_2 in Supercritical Water. *Ind. Eng. Chem. Res.* **2012**, *51*,
12253–12257.
- (11) Liebig, C.; Paul, S.; Katryniok, B.; Guillon, C.; Couturier, J. L.;
Dubois, J. L.; Dumeignil, F.; Hoelderich, W. F. Glycerol Conversion to
Acrylonitrile by Consecutive Dehydration over WO_3/TiO_2 and
Amoxidation over Sb-(Fe,V)-O. *Appl. Catal., B* **2013**, *132*, 170–182.
- (12) Do, Y. R.; Lee, W.; Dwight, K.; Wold, A. The Effect of WO_3 on
the Photocatalytic Activity of TiO_2 . *J. Solid State Chem.* **1994**, *108*,
198–201.
- (13) Keller, V.; Bernhardt, P.; Garin, F. Photocatalytic Oxidation of
Butyl Acetate in Vapor Phase on TiO_2 , Pt/ TiO_2 and WO_3/TiO_2
Catalysts. *J. Catal.* **2003**, *215*, 129–138.
- (14) Puddu, V.; Mokaya, R.; Puma, G. L. Novel One Step
Hydrothermal Synthesis of TiO_2/WO_3 Nanocomposites with
Enhanced Photocatalytic Activity. *Chem. Commun.* **2007**, 4749–4751.
- (15) Sajjad, A. K. L.; Shamaila, S.; Tian, B. Z.; Chen, F.; Zhang, J. L.
One Step Activation of WO_x/TiO_2 Nanocomposites with Enhanced
Photocatalytic Activity. *Appl. Catal., B* **2009**, *91*, 397–405.
- (16) Yang, L. Y.; Si, Z. C.; Weng, D.; Yao, Y. W. Synthesis,
Characterization and Photocatalytic Activity of Porous WO_3/TiO_2
Hollow Microspheres. *Appl. Surf. Sci.* **2014**, *313*, 470–478.
- (17) Tsukamoto, D.; Ikeda, M.; Shiraishi, Y.; Hara, T.; Ichikuni, N.;
Tanaka, S.; Hirai, T. Selective Photocatalytic Oxidation of Alcohols to

- 735 Aldehydes in Water by TiO₂ Partially Coated with WO₃. *Chem.—Eur. J.* **2011**, *17*, 9816–9824.
- 736 (18) Szilagyi, I. M.; Forizs, B.; Rosseler, O.; Szegedi, A.; Nemeth, P.; Kiraly, P.; Tarkanyi, G.; Vajna, B.; Varga-Josepovits, K.; Laszlo, K.; Toth, A. L.; Baranyai, P.; Leskela, M. WO₃ Photocatalysts: Influence of Structure and Composition. *J. Catal.* **2012**, *294*, 119–127.
- 741 (19) Ramos-Delgado, N. A.; Gracia-Pinilla, M. A.; Maya-Trevino, L.; Hinojosa-Reyes, L.; Guzman-Mar, J. L.; Hernandez-Ramirez, A. Solar Photocatalytic Activity of TiO₂ Modified with WO₃ on the Degradation of an Organophosphorus Pesticide. *J. Hazard. Mater.* **2013**, *263*, 36–44.
- 746 (20) Ramos-Delgado, N. A.; Hinojosa-Reyes, L.; Guzman-Mar, I. L.; Gracia-Pinilla, M. A.; Hernandez-Ramirez, A. Synthesis by Sol-Gel of WO₃/TiO₂ for Solar Photocatalytic Degradation of Malathion Pesticide. *Catal. Today* **2013**, *209*, 35–40.
- 750 (21) Luevano-Hipolito, E.; Martinez-de la Cruz, A.; Lopez-Cuellar, E.; Yu, Q. L.; Brouwers, H. J. H. Synthesis, Characterization and Photocatalytic Activity of WO₃/TiO₂ for NO Removal under UV and Visible Light Irradiation. *Mater. Chem. Phys.* **2014**, *148*, 208–213.
- 754 (22) Patrocino, A. O. T.; Paula, L. F.; Paniago, R. M.; Freitag, J.; Bahnemann, D. W. Layer-by-Layer TiO₂/WO₃ Thin Films as Efficient Photocatalytic Self-Cleaning Surfaces. *ACS Appl. Mater. Interfaces* **2014**, *6*, 16859–16866.
- 758 (23) Zhu, Y.; Su, X. T.; Yang, C.; Gao, X. Q.; Xiao, F.; Wang, J. D. Synthesis of TiO₂-WO₃ Nanocomposites as Highly Sensitive Benzene Sensors and High Efficiency Adsorbents. *J. Mater. Chem.* **2012**, *22*, 13914–13917.
- 762 (24) Miller, D. R.; Akbar, S. A.; Morris, P. A. Nanoscale Metal Oxide-Based Heterojunctions for Gas Sensing: A Review. *Sens. Actuators, B* **2014**, *204*, 250–272.
- 765 (25) Yang, X. L.; Dai, W. L.; Guo, C. W.; Chen, H.; Cao, Y.; Li, H. X.; He, H. Y.; Fan, K. N. Synthesis of Novel Core-Shell Structured WO₃/TiO₂ Spheroids and Its Application in the Catalytic Oxidation of Cyclopentene to Glutaraldehyde by Aqueous H₂O₂. *J. Catal.* **2005**, *234*, 438–450.
- 770 (26) de Castro, I. A.; Avansi, W.; Ribeiro, C. WO₃/TiO₂ Heterostructures Tailored by the Oriented Attachment Mechanism: Insights from Their Photocatalytic Properties. *CrystEngComm* **2014**, *16*, 1514–1524.
- 774 (27) Riboni, F.; Bettini, L. G.; Bahnemann, D. W.; Selli, E. WO₃-TiO₂ Vs. TiO₂ Photocatalysts: Effect of the W Precursor and Amount on the Photocatalytic Activity of Mixed Oxides. *Catal. Today* **2013**, *209*, 28–34.
- 778 (28) Epifani, M.; Diaz, R.; Force, C.; Comini, E.; Andreu, T.; Zamani, R. R.; Arbiol, J.; Siciliano, P.; Faglia, G.; Morante, J. R. Colloidal Counterpart of the TiO₂-Supported V₂O₅ System: A Case Study of Oxide-on-Oxide Deposition by Wet Chemical Techniques. Synthesis, Vanadium Speciation, and Gas-Sensing Enhancement. *J. Phys. Chem. C* **2013**, *117*, 20697–20705.
- 784 (29) Epifani, M.; Andreu, T.; Arbiol, J.; Diaz, R.; Siciliano, P.; Morante, J. R. Chloro-Alkoxide Route to Transition Metal Oxides. Synthesis of WO₃ Thin Films and Powders from a Tungsten Chloro-Methoxide. *Chem. Mater.* **2009**, *21*, 5215–5221.
- 788 (30) Epifani, M.; Comini, E.; Faglia, G.; Arbiol, J.; Andreu, T.; Pace, G.; Siciliano, P.; Morante, J. R. Two Step, Hydrolytic-Solvothermal Synthesis of Redispersible Titania Nanocrystals and Their Gas-Sensing Properties. *J. Sol-Gel Sci. Technol.* **2011**, *60*, 254–259.
- 792 (31) Epifani, M.; Comini, E.; Diaz, R.; Andreu, T.; Genç, A.; Arbiol, J.; Siciliano, P.; Faglia, G.; Morante, J. R. Solvothermal, Chloroalkoxide-Based Synthesis of Monoclinic WO₃ Quantum Dots and Gas-Sensing Enhancement by Surface Oxygen Vacancies. *ACS Appl. Mater. Interfaces* **2014**, *6*, 16808–16816.
- 797 (32) Daniel, M. F.; Desbat, B.; Lassegues, J. C.; Gerand, B.; Figlarz, M. Infrared and Raman-Study of WO₃ Tungsten Trioxides and WO₃·xH₂O Tungsten Trioxide Hydrates. *J. Solid State Chem.* **1987**, *67*, 235–247.
- 801 (33) Salvati, L.; Makovsky, L. E.; Stencel, J. M.; Brown, F. R.; Hercules, D. M. Surface Spectroscopic Study of Tungsten-Alumina Catalysts Using X-Ray Photoelectron, Ion Scattering, and Raman Spectroscopies. *J. Phys. Chem.* **1981**, *85*, 3700–3707.
- 804 (34) Horsley, J. A.; Wachs, I. E.; Brown, J. M.; Via, G. H.; Hardcastle, F. D. Structure of Surface Tungsten Oxide Species in the Tungsten Trioxide/Alumina Supported Oxide System from X-Ray Absorption near-Edge Spectroscopy and Raman Spectroscopy. *J. Phys. Chem.* **1987**, *91*, 4014–4020.
- 809 (35) Deo, G.; Wachs, I. E. Predicting Molecular-Structures of Surface Metal-Oxide Species on Oxide Supports under Ambient Conditions. *J. Phys. Chem.* **1991**, *95*, 5889–5895.
- 812 (36) Vuurman, M. A.; Wachs, I. E.; Hirt, A. M. Structural Determination of Supported V₂O₅-WO₃/TiO₂ Catalysts by in Situ Raman-Spectroscopy and X-Ray Photoelectron-Spectroscopy. *J. Phys. Chem.* **1991**, *95*, 9928–9937.
- 816 (37) Ramis, G.; Busca, G.; Cristiani, C.; Lietti, L.; Forzatti, P.; Bregani, F. Characterization of Tungsta-Titania Catalysts. *Langmuir* **1992**, *8*, 1744–1749.
- 819 (38) Scholz, A.; Schnyder, B.; Wokaun, A. Influence of Calcination Treatment on the Structure of Grafted WO₃ Species on Titania. *J. Mol. Catal. A: Chem.* **1999**, *138*, 249–261.
- 822 (39) Reiche, M. A.; Burgi, T.; Baiker, A.; Scholz, A.; Schnyder, B.; Wokaun, A. Vanadia and Tungsta Grafted on TiO₂: Influence of the Grafting Sequence on Structural and Chemical Properties. *Appl. Catal., A* **2000**, *198*, 155–169.
- 826 (40) Yu, X.-F.; Wu, N.-Z.; Huang, H.-Z.; Xie, Y.-C.; Tang, Y.-Q. A Study on the Monolayer Dispersion of Tungsten Oxide on Anatase. *J. Mater. Chem.* **2001**, *11*, 3337–3342.
- 829 (41) Barreca, D.; Carta, G.; Gasparotto, A.; Rossetto, G.; Tondello, E.; Zanella, P. A Study of Nanophase Tungsten Oxides Thin Films by XPS. *Surf. Sci. Spectra* **2001**, *8*, 258–267.
- 832 (42) Jeon, S.; Yong, K. Synthesis and Characterization of Tungsten Oxide Nanorods from Chemical Vapor Deposition-Grown Tungsten Film by Low-Temperature Thermal Annealing. *J. Mater. Res.* **2008**, *23*, 1320–1326.
- 836 (43) Grabowska, E.; Sobczak, J. W.; Gazda, M.; Zaleska, A. Surface Properties and Visible Light Activity of W-TiO₂ Photocatalysts Prepared by Surface Impregnation and Sol-Gel Method. *Appl. Catal., B* **2012**, *117–118*, 351–359.
- 839 (44) Silversmit, G.; Doncker, G. D.; Gryse, R. D. A Mineral TiO₂ (001) Anatase Crystal Examined by XPS. *Surf. Sci. Spectra* **2002**, *9*, 21–29.
- 843 (45) Marcus, B.; Fayette, L.; Mermoux, M.; Abello, L.; Lucazeau, G. Analysis of the Structure of Multicomponent Carbon-Films by Resonant Raman-Scattering. *J. Appl. Phys.* **1994**, *76*, 3463–3470.
- 846 (46) Stair, P. C.; Li, C. Ultraviolet Raman Spectroscopy of Catalysts and Other Solids. *J. Vac. Sci. Technol., A* **1997**, *15*, 1679–1684.
- 847 (47) Tuinstra, F.; Koenig, J. L. Raman Spectrum of Graphite. *J. Chem. Phys.* **1970**, *53*, 1126–1130.
- 850 (48) Lee, D. H.; Condrate, R. A. FTIR Spectral Characterization of Thin Film Coatings of Oleic Acid on Glasses: I. Coatings on Glasses from Ethyl Alcohol. *J. Mater. Sci.* **1999**, *34*, 139–146.
- 853 (49) Yu, W. W.; Wang, Y. A.; Peng, X. G. Formation and Stability of Size-, Shape-, and Structure-Controlled CdTe Nanocrystals: Ligand Effects on Monomers and Nanocrystals. *Chem. Mater.* **2003**, *15*, 4300–4308.
- 857 (50) Young, A. G.; Al-Salim, N.; Green, D. P.; McQuillan, A. J. Attenuated Total Reflection Infrared Studies of Oleate and Trioctylphosphine Oxide Ligand Adsorption and Exchange Reactions on CdS Quantum Dot Films. *Langmuir* **2008**, *24*, 3841–3849.
- 861 (51) Deacon, G. B.; Phillips, R. J. Relationships between the Carbon-Oxygen Stretching Frequencies of Carboxylate Complexes and the Type of Carboxylate Coordination. *Coord. Chem. Rev.* **1980**, *33*, 227–250.
- 865 (52) Yamazoe, N.; Shimano, K. Theory of Power Laws for Semiconductor Gas Sensors. *Sens. Actuators, B* **2008**, *128*, 566–573.
- 867 (53) Kohl, D. Surface Processes in the Detection of Reducing Gases with SnO₂-Based Devices. *Sens. Actuators, B* **1989**, *18*, 71–113.
- 869

- 870 (54) Gurlo, A.; Riedel, R. In Situ and Operando Spectroscopy for
871 Assessing Mechanisms of Gas Sensing. *Angew. Chem., Int. Ed.* **2007**, *46*,
872 3826–3848.
- 873 (55) Epifani, M.; Andreu, T.; Zamani, R.; Arbiol, J.; Comini, E.;
874 Siciliano, P.; Faglia, G.; Morante, J. R. Pt Doping Triggers Growth of
875 TiO₂ Nanorods: Nanocomposite Synthesis and Gas-Sensing Proper-
876 ties. *CrystEngComm* **2012**, *14*, 3882–3887.